# Powerful amorphous mixed metal catalyst for efficient water-oxidation

Geraldine Merle, Isaac Abrahams, Jake Barralet*

Dr. G. Merle

Department of Chemical Engineering, McGill University, Montreal, H3A 0C5, Canada

Dr. I. Abrahams

School of Biological and Chemical Sciences, Queen Mary University of London, Mile End Road, London, E1 4NS, United Kingdom

Prof. J. E. Barralet

E-mail: jake.barralet@mcgill.ca

Faculty of Medicine, McGill University, Montreal, Canada

Faculty of Dentistry, McGill University, Montreal, H3A 2B2, Canada

Keywords: Oxygen evolution reaction, cobalt, vanadium, water oxidation, alkaline, neutral, catalysis

One of the greatest challenges of our era is the splitting of water in a cheap and effective way to produce an abundance of clean hydrogen fuel in order to sustain current levels of energy consumption. Today, Oxygen Evolution Reaction (OER) electrode materials are largely based on rare earth elements $RuO_2$ and $IrO_2$, which are increasingly scarce. Here, we report the discovery of an inexpensive new material based on oxides of cobalt and vanadium that exhibits excellent stability under alkaline water electrolysis conditions and the lowest

overpotentials reported to date for OER in both neutral and alkaline conditions. This material outperforms $IrO_2$ and a recently discovered cobalt phosphate catalyst in terms of both OER catalytic activity and long-term materials stability associated with a low overpotential.

## 1. Introduction

Efficient water splitting, through the electrolysis of water into hydrogen ($H_2$) and oxygen ($O_2$), is a key challenge in renewable electrical energy storage. The oxygen evolution reaction (OER), creates a double O-O bond from two water molecules thereby releasing four protons and four electrons. This is not an energetically favourable reaction and so requires a large overpotential[1,2]. Water electrolysers require extreme pH to favour this reaction and perform water splitting in 6 to 9 M KOH on nickel electrodes at around 80-90 °C[3-5]. These are simple designs that are relatively cheap, but are not particularly efficient. As a consequence, electrolysers are large and have considerable energy requirements, since they contain hot and caustic liquid and represent a safety concern for inhabited spaces. More efficient and smaller electrolysers that operate at lower temperature rely on expensive cationic membrane technologies and $IrO_2$ electrodes,[6] that are typically used where space or safety is a primary consideration. Oxides and hydroxides of iridium and ruthenium exhibit good electrocatalytic activity towards the OER with a low overpotential and high current density. They have long been used as anodes in electrocatalytic systems for OER despite their high cost[7,8] and $IrO_2$ is the best performing electrocatalyst discovered to date for the OER. There is an absence of competitive low cost catalytic materials with high current densities ($j$) (> 0.5 A $cm^{-2}$) at low overpotentials ($\eta < 0.3$ V) over prolonged time periods[2] and this impedes the development of small, efficient water fueled hydrogen and oxygen generators.

Oxides of Mn, Co, Ni and Fe[9-13] have been found to be satisfactory, but not particularly efficient OER catalysts. $Co_3O_4$[14-16] and the substituted cobaltite oxides $M_xCo_{3-x}O_4$ (M = Ni, Fe,

Cu or Zn)[17,18] also exhibit promising OER performances with fairly good stability in alkaline media compared to $RuO_2$ and $IrO_2$[6]. Together, the low conductivity of $Co_3O_4$ ($10^{-4}$ S $cm^{-2}$ compared to 1-2 $\times$ $10^{-4}$ S $cm^{-2}$ for $RuO_2$ and $IrO_2$)[19] leading to poor charge transport through the catalyst film combined with the corrosiveness of the alkaline solution obstruct the development and commercialization of cobalt oxide as an OER electrocatalyst [20-24].

Recently, amorphous oxides such as cobalt-phosphate[25,26], cobalt-borate[27], and $RuO_2$[28] have generated interest because of their promising catalytic activity for water oxidation in alkaline as well as neutral conditions, but their performance is still low for competing alkaline or acidic electrolysers[25]. Altering the electrical conductivity can be achieved with dopants or defects in order to increase the mobile carrier density. For example, Ni-doped $Co_3O_4$ nanowires showed improved electrocatalytic activity with a higher current density at the same overpotential compared to the undoped $Co_3O_4$ [18]. This increase of performance was attributed to an increase in the carrier number, higher surface area and improved electrical conductivity by four orders of magnitude (0.6 S $cm^{-1}$)[18,29]. Vanadium dioxide ($VO_2$) interestingly displays an insulator-conductor transition at around 70 °C whereupon it metallizes and its electrical conductivity abruptly increases by $10^4$ orders of magnitude. Doping $VO_2$ with transition metal ions, such as tungsten[30,31], niobium[32,33], molybdenum[34], titanium[35], has been shown to modulate the thermal and electrical conductivities i) to reduce the transition temperature and ii) to increase room temperature conductivity .

Here we report the first example of a mixed amorphous cobalt-vanadium OER electrocatalyst with the lowest overpotential in the pH range 14-7. Despite having a very low specific surface area, zero porosity and large (> 1.5 µm) particle size, these amorphous electrocatalysts interestingly performed better than any reported electrocatalyst at these pH values. This

finding potentially removes one of the remaining obstacles to high efficiency water-oxidation using inexpensive and earth-abundant materials.

## 2. Materials and methods

### 2.1. *Materials*

Citric acid anhydrous, glycine (99%), vanadium(IV) oxide sulfate hydrate (97%), and cobalt(II) nitrate hexahydrate (98%) were purchased from Sigma Aldrich, potassium hydroxide (85%) and potassium phosphate monobasic and dibasic were purchased from Fisher. All electrolyte solutions were prepared with Milli-Q water (18.2 MΩ $cm^{-1}$) obtained from an AquaMax-Ultra apparatus.

### 2.2. *Materials synthesis*

The electrocatalysts were prepared by citrate–nitrate auto-combustion (CNA) synthesis with citric acid as fuel[36]. Here citric acid is the fuel as well as the complexing agent, whereas the metal nitrate is the metal ion and oxidant source. Because this reaction is a low-temperature process, nitrate is not eliminated as $NO_x$, but remains in the mixture and causes the metal-citrate to auto-combust. Required amounts of metal nitrate, vanadyl sulfate and citric acid (cobalt nitrate: citric acid molar ratio; 1:1 and cobalt nitrate: vanadyl sulfate mass ratios with for example 5:1 for the Co-V 5:1 sample) were weighed to the nearest milligram and dissolved in milliQ water. For Co-V electrocatalyst preparation, cobalt nitrate and vanadyl sulfate were first mixed together. After complete dissolution, citric acid was added to the mixture, and then the aqueous solution was heated on a hotplate at about 80 °C to evaporate the excess of water. Finally, the obtained foam was further dried at 120 °C for 20 hours in a static air atmosphere followed by calcination at 250 °C for 5 hours. CoPI catalyst films were electrodeposited on glassy carbon electrodes by controlled potential electrolysis of a 0.5 mM $Co(NO_3)_2$ aqueous solution in 100 mM potassium phosphate buffer at pH 7.0. The electrolysis

was carried out at 0.85 V (vs. Ag/AgCl) for 5 hours. $Co_3O_4$ catalyst was prepared by mixing citric acid with cobalt nitrate at a cobalt nitrate: citric acid molar ratio of 1:1, in milliQ water. After complete dissolution, the water was removed on a hotplate at 80 °C, followed by 20 hours in a furnace at 120 °C and finally 5 hours at 250 °C.

### 2.3. *Electrochemical methods*

The electrochemical studies were carried out with a potentiostat VersaSTAT 3 (Princeton Applied Research) using a three-electrode electrochemical cell consisting of 50 mL of electrolyte solution. The experiments were performed at ambient temperature, the potentials were converted to the NHE following E(NHE) = E(SCE) + 0.240 V and the overpotentials were calculated using $\eta$ = E(NHE) – 0.4 V. Unless otherwise stated, the electrolyte was 1 M potassium hydroxide, pH 14.

#### 2.3.1. *Temperature dependence study*

The electrochemical cell was immersed in a silicon oil bath and the temperature of the oil bath was gradually increased. Temperature was measured with a thermometer inserted in the electrochemical cell. At specific temperature (4, 22, and 70 °C), electrochemical measurement was performed.

#### 2.3.2. *Cyclic voltammetry*

A 0.12 $cm^2$ glassy carbon electrode was used as the working electrode and Pt wire as the counter electrode. The working electrode was polished for at least 1 minute with 0.05 μm alumina particles and sonicated 5 minutes in water and isopropanol prior to use. Cyclic voltammograms were collected at 20 mV $s^{-1}$ in KOH electrolyte. Current-potential curves were recorded in 1M KOH electrolyte at a variety of applied potentials starting at 0.3 V proceeding at 1 mV $s^{-1}$.

#### 2.3.3. *Calculation of turnover frequency*

Turnover frequency (TOF) values were calculated according to the equation[37]: $TOF = j \times A/(4 \times F \times m)$, where $j$ is the current density obtained at 400 mV in A $cm^{-2}$, $A$ is the surface area of the electrode (0.07 $cm^{-2}$), $F$ is Faraday efficiency (96485 C $mol^{-1}$) and $m$ is the number of moles of Co deposited onto the GC electrodes.

2.4. *Methods*

The morphology was investigated with Scanning Electron Microscopy using an SEM FEG Quanta Scanning Electron Microscope (Inspect F50, FEI Company, Hillsboro, OR, USA) with an EDAX Octane super 60 $mm^2$ SDD EDS analysis system and Transmission Electron Microscopy (TEM) (Philips CM20). X-ray diffraction (XRD) analysis was carried out on a Bruker D8 Discovery instrument operating at 40 kV and 20 mA, using Cu-Kα radiation. Elemental composition and atomic bonding information were studied with X-ray Photo-electron Spectroscopy (XPS, Thermo Scientific K-Alpha) with an Al Kα micro-focused monochromator, and Energy Dispersive X-ray analysis spectroscopy (EDS). Gas chromatography analysis with performed with a gas chromatograph SRI GC 8610.The Brunauer-Emmett-Teller (BET) method was used for the specific surface area (SSA) (Tristar 3000, Micromeritics Instrument Corporation Norcross, Georgia, USA) by nitrogen adsorption and desorption.

## 3. Results and discussion

### 3.1. Electrochemical evaluation of Co-V electrocatalyst

The current density of a Co-V catalyst on a GC electrode was measured as a function of the overpotential (η) in KOH electrolyte. At pH 14.0 (**Figure 1A)**, a large catalytic current was measured beginning at η = 300 mV, with a current density of 10 mA $cm^{-2}$ at η = 310 mV associated with OER despite the low surface area (< 0.01 $m^2 g^{-1}$) of the sample. By comparison, the $Co_3O_4$ control had a catalytic current beginning at η = 450 mV, and a current

density of 10 mA $cm^{-2}$ at $\eta$ = 490 mV and a surface area of approximately 30 $m^2 g^{-1}$. This increase in catalytic current may originate from the vanadium insertion into the Co framework. A similar effect with an increased current of 1.6 and 4 times higher than that of undoped $Co_3O_4$ samples has been observed with $Li^{2+}$ , [38] $Zn^{2+}$ [39] and $Ni^{2+}$ [39] ion insertion. Incorporating these ions in the $Co_3O_4$ lattice resulted in a change of the $Co_3O_4$ electronic structure that enhanced the adsorption of $OH^-$ and thus facilitated the oxidation of $Co^{3+}$ as follows: CoOOH + $OH^- \rightarrow CoO_2 + H_2O + e^-$, creating more $Co^{4+}$ species as active centers for advanced OER activity. The overpotential to reach a current density of 10 mA $cm^{-2}$ of Co-V electrocatalysts was compared to other state of the art OER electrocatalysts, as suggested previously as a means to evaluate water splitting OER catalysts [10] (Supplementary Information, **Figure S1**). The 5:1 Co-V electrocatalyst is located to the left side of the graphic close to the diagonal dashed line, which is the ideal response for a stable catalyst in alkaline condition[6,10]. In comparison with other metal oxides known for OER electrocatalysis, such as $Co_3O_4$ supported graphene catalyst[40] (onset potential at 0.406V), $Co_3O_4$/SWNTs (onset potential at 593 mV), $Co_3O_4$ nano-islands (376 mV at 10 mA $cm^{-2}$)[41], mesoporous $Co_3O_4$ catalysts (onset potential at 525 mV), graphene/$Co_3O_4$ catalysts (onset potential at 310 mV),[42-44] $IrO_2$ (411 mV)[45] or $RuO_2$ (358 mV)[10], the Co-V material reported here has superior electrocatalytic behavior for OER. Besides exhibiting a much lower onset potential than the $RuO_2$ and $IrO_2$ electrocatalysts, Co-V catalyst exhibited higher current densities at lower potentials. This is especially significant considering the price of Co and V currently at < $12 per lb and ~$7000 and $3000 per lb for Ir and Ru respectively). The effect of V- doping on Co electrocatalysts was assessed with linear sweep voltammetry in alkaline conditions at various temperatures (**Figure 1B**). From 4 °C to 70 °C, the anodic current rapidly increased by 80% from 100 to 180 mA $cm^{-2}$ at $\eta$ = 600 mV for Co-V, whereas that for $Co_3O_4$ electrodes increased by 67% from 30 to 50 mA $cm^{-2}$.

**Figure 1. (A)** Cyclic voltammograms of $Co_3O_4$ control catalyst and Co-V catalyst. The x-axis is the overpotential vs. Ag/AgCl and y-axis represents the current density in mA $cm^{-2}$, at 20 mV $s^{-1}$ in 1 M KOH at 25 °C. **(B)** Temperature dependence of the catalytic current for Co control catalyst and Co-V catalyst in 1 M KOH. **(C)** Chronopotentiometric plot of Co control catalyst and Co-V catalyst at 10 mA $cm^{-2}$ in 1 M KOH at 25 °C. **(D)** Linear sweep voltammetry at a scan rate of 20 mV s, in 0.1 M phosphate buffer pH 7.4 at 25 °C.

To further understand the catalytic properties for OER of the Co-V electrocatalyst, a Tafel plot analysis was performed derived from the polarization curves using the Tafel equation $\eta$ = b log($j/j_0$), where $\eta$ is the overpotential, b is the Tafel slope, $j$ is the current density, and $j_0$ is the exchange current density (Supplementary Information, **Figure S2A**). The Co-V electrode had a Tafel slope of 66 mV $dec^{-1}$, whereas the $Co_3O_4$ control exhibited a Tafel slope of 79 mV $dec^{-1}$. In comparison with Tafel slopes reported in the literature, such as those for reduced $Co_3O_4$ porous nanowires (72 mV $dec^{-1}$) [46], hollow 'fluffy' cages of $Co_3O_4$ (70 mV $dec^{-1}$)[47], $Co_3O_4$ nanoparticles (78 mV $dec^{-1}$), $Co_3O_4$ nanocrystals on graphene (68 mV $dec^{-1}$)[43], cobalt carbonate hydroxide/C (116 mV $dec^{-1}$)[48], and nanoporous hollow $Co_3S_4$ (90 mV $dec^{-1}$)[49], the lower value obtained for Co-V suggests a remarkable electrocatalytic activity for OER probably from the coupling of vanadium with cobalt that might create more active sites with larger charge transfer coefficients[50]. The electrocatalytic characterization of the Co-V catalyst vs. $Co_3O_4$ was conducted via electrochemical impedance spectroscopy at a current density of 10 mA $cm^{-2}$ where the OER has already proceeded. The Nyquist plots of the Co-V and $Co_3O_4$ electrodes (Supplementary Information, **Figure S2B**), clearly display a semi-circle with a slight distortion at high frequency, resulting from the catalytic film itself [51]. The larger arc at lower frequencies is attributed to the OER resistances [51]. The charge transfer resistance associated with the OER can be calculated from the diameter of the large semi-circle. From **Figure S2B**, given in the Supplementary Information, it is apparent that the charge transfer

resistance of the Co-V electrode is drastically reduced, indicating a lower resistance and an easier electro-oxidative process. The turnover frequency (TOF) of the Co-V sample was calculated assuming that all the Co sites were involved in OER. We calculated a TOF of 0.061 $s^{-1}$ at an overpotential of 400 mV, to produce anodic current densities of 10 mA $cm^{-2}$; almost 100 times lower than that of $IrO_2$[52], three times higher than that of Ir/ C (0.027 $s^{-1}$)[53] and approximately ten higher than in cobalt oxides and (oxy)hydroxides[54].

To establish that the catalytic activity observed with the Co-V material is only due to the water splitting and that $O_2$ produced comes only from water, electrolysis was performed in helium saturated KOH electrolyte. During the experiment, helium gas was constantly flowed through the headspace of the anodic compartment and the gas produced at the anode was collected and analyzed with gas chromatography. The result shows that only $O_2$ gas was generated during the electrolysis with no-side reaction of unwanted gas.

The durability of the OER electrocatalysts at an applied current density of 10 mA $cm^{-2}$ at pH = 14 was assayed by chronocoulometry (**Figure 1C**). Interestingly, while OER activity of the $Co_3O_4$ electrocatalyst decreased with time in alkaline medium, the OER activity of the Co-V catalyst gradually enhanced in alkaline media with time (5 h) by 8% (**Figure 1C**). The morphology, elemental composition and crystallinity of the electrocatalysts after the durability test appear unchanged (Supplementary Information, **Figure S3**). Since long-term stability in real conditions is a key parameter for any potential use in an electrolyzer, the stability of the Co-V catalyst was also measured by incubating the electrocatalyst in 6 M KOH solution at 80 °C, and by periodically monitoring its activity (Supplementary Information, **Figure S4)**. The catalyst maintained ~50% of its initial activity after 2 months.

Oxygen evolution in neutral solutions is extremely attractive due to its benign nature and lower causticity [25]. While the electrocatalytic activity of the Co control and Co-V catalyst towards OER is drastically impeded in neutral conditions, the Co-V electrocatalyst could easily operate. Obviously the OER onset potential shifted towards a higher voltage compared to that in an alkaline environment, nevertheless the catalytic current of the Co-V catalyst is seven times higher (3.5 mA $cm^{-2}$ vs. 0.5 mA $cm^{-2}$ at 1.1 V) than the well documented CoPi electrocatalyst[25], OER reference in neutral conditions (**Figure 1D).**

### 3.2. Preparation and characterization of the electrocatalysts

The method of preparation of metal oxides strongly impacts their surface area; generally high calcining temperatures promote larger crystallite size and low surface area[55]. Citric acid as chelating agent and fuel and cobalt nitrates as oxidants were used at low temperature (below 300 °C) to produce Co-V nanopowders [36]. Prior to the incorporation of citric acid, the vanadyl sulfate was mixed with cobalt nitrate until complete dissolution in water. After drying the resultant solution to yield a dried foam, subsequent pyrolysis led to the formation of a solid foam (**Figure 2A**). The calcined foams formed after 5 hours at 250 °C, but the Co and Co-V oxides had distinct appearances (**Figure 2B**): a brittle electrostatic black foam and a brown and shiny metallic looking foam for the control and the Co-V electrocatalysts, respectively. The LSV data for other ratios of Co-V electrocatalysts are shown in **Figures S5A**. SEM pictures of Co-V catalysts at different ratios. Particles exhibited an irregular shape suggestive of a glassy material and that the insertion of V appeared to increase the size of particles from 500 nm to 1.5 μm (**Figures S5C)**. As the amount of vanadyl salts increased, the OER efficiency of the resulting catalysts increased. It shows that the Co-V catalysts exhibit a significantly higher catalytic current than control catalyst, with an OER onset overpotential of

around 0.3 V and 0.4 V for Co-V catalyst and Co control respectively. The mass ratio 5:1 $Co(NO_3)_2$:$VOSO_4$ seems to produce more electro catalytically active materials towards OER.

**Figure 2**. **(A)** Top to bottom (Left: control and Right: Co-V): Starting solutions, after the 1st drying step and finally the calcined foam obtained after pyrolysis. **(B)** Pictures of the final electrocatalytic material (top: control and bottom: Co-V). **(C)** SEM micrographs of the control and **(D)** Co-V catalysts. Elemental mapping of the Co-V materials with (E, yellow) Co and (F, blue) V elements. The elemental map signals were obtained by scanning a square of the Co-V image.

Scanning electron microscopy (SEM) and associated elemental mapping indicated a uniform distribution of Co and V for the sample calcined at 250 °C (**Figure 2E-F)**. The surface of the control is grainy and appears to be an agglomerate of nanoparticles (**Figure 2**), whereas the surface of the Co-V catalyst consists of smooth fragments in the microscale range (**Figure 2D**). The specific surface area (SSA) of the Co-V material, confirmed the lack of porosity in this material as the surface area was too low to be measured by either nitrogen or argon adsorption. Energy-dispersive X-ray analysis (EDX) spectra were obtained from multiple regions of SEM samples and identified Co, V and O as the principal elemental components (Supplementary Information, **Figure S6**). Elemental mapping was suggestive of the existence of an even dispersion of V and Co rich nano-domains. Elemental analysis with X-ray fluorescence of the material indicated it was composed mainly of Co, O and V (30.7, 22.7, and 19.9 wt. % respectively), with lesser amounts of C, N, S and P (15.4, 7.8, 2.8 and 0.3 wt.% respectively).

FTIR spectra for both the control and Co-V electrocatalyst manifest the presence of two absorption bands at 570 ($\upsilon_1$) and 661($\upsilon_2$) $cm^{-1}$, which originate from the stretching vibrations of the metal-oxygen bond and indicate the formation of $Co_3O_4$ spinel oxide in both samples (**Figure 3A**). The $\upsilon_1$ band is characteristic of $OB_3$ (where B denotes the $Co^{3+}$ in the octahedral hole) vibration and the $\upsilon_2$ band is attributable to the $ABO_3$ (where A denotes the $Co^{2+}$ in the tetrahedral hole) vibration in the spinel lattice[56].

**Figure 3. (A)** FTIR of Co-V catalyst and Co control catalyst before (a and c) and after (b and d) heat treatment at 600˚C, **(B)** XRD of Co-V catalyst (XRD of Co-control catalyst in Supplementary Information, **Figure S6** A), **(C)** XPS survey and **(D)** XPS spectra of the Co element.

Furthermore, the Co-V electrocatalyst spectra exhibit two additional characteristic absorption bands at 756 and 1080 $cm^{-1}$ related to the asymmetric stretching vibrations of V-O-V units and the symmetric V= O stretch respectively[57]. After 1 hour at 600 °C, the two absorption bands of the metal-oxygen bond of the Co disappeared in the Co-V materials, whereas the spectra of the $Co_3O_4$ control remained unchanged. The X-ray diffraction (XRD) pattern of the $Co_3O_4$ control were in good agreement with the standard pattern for well-crystallized cubic spinel $Co_3O_4$ (JCPDS card file no. 80-1545) (**Figure S7A**). The XRD pattern for the Co-V catalyst is shown in **Figure 3**. The pattern confirms a highly amorphous material with a broad peak 2θ at ca. 12° 2θ. Bragg peaks corresponding to $Co_3O_4$ are also evident alongside those tentatively identified as vanadyl sulfate pentahydrate, $VOSO_4.5H_2O$ (JCPDS 19-1414). However, it should be noted that the JCPDS reference pattern for the latter phase is questionable and is believed to a combination of multiple phases. The XRD pattern of the Co-V catalyst post annealing is significantly different to that prior to annealing. The $Co_3O_4$ spinel peaks are absent and replaced by those of $Co(SO_4)_4$ (JCPDS card file no. 38-386). Due to the

weakness of the Bragg peaks in the pattern (exarcerbated by Co fluorescence), only tentative assignments can be made for the other species including $VOHSO_4$ (28-1435), $VO_{1.75}(OH)_{0.25}$ (37-503) and $VO_2$ (25-1003) (**Figure S7B**). The Bragg peaks in the XRD patterns of both the un-annealed Co-V and annealed Co-$V_{600°C}$ samples were broad indicating that the size of Co-V and Co-$V_{600°C}$ crystalline regions are small. The XPS survey spectrum of the Co-V sample shows the Co 2*p*, V 2*p*, C 1*s*, S 2*p* and O 1*s* XPS peaks (**Figure 3C)**. As shown in **Figure 3D**, in the Co region, two broad sets of signals corresponding to the $2p_{3/2}$ (782.2 eV) and $2p_{1/2}$ (798 eV) core levels with a spin energy separation of 15.8 eV were observed, making the presence of metallic cobalt (778.0 eV) or cobalt oxides (780 eV) such as $Co_3O_4$ (**Figure S7D**) or CoO at the surface of the Co-V catalyst improbable. Furthermore, the two peaks at 781.5 and 787.5 eV were attributed to $Co^{III}_{3/2}$ and $Co^{II}_{3/2}$ with a high $Co^{III}_{3/2}$/ $Co^{II}_{3/2}$ ratio (~6), indicating a surface excess of $Co^{3+}$, favorable for the OER.

TEM images of the Co-V catalyst showed an irregular shape suggestive of a glassy material. Where particles were small enough to allow electron transmission, there was some evidence of a flake or plate-like morphology in smaller particles. (**Figure 4A**) EDX analysis demonstrated that these platelets are made of the elements Co, O, V and S from the sulfate of the vanadyl source (**Figure 4B**).

**Figure 4**. TEM images of a Co-V sample, **(A)** Low magnification TEM image of a Co-V sample, **(B)** representative EDS spectrum and **(C)** HR-TEM image of an individual platelet. **(D)** HRTEM image of an individual platelet after 10 h subjected to electrolysis.

A high resolution TEM picture of an individual platelet is shown in **Figure 4C.** Selected area electron diffraction (SAED) patterns collected from this platelet architecture confirm its amorphous nature (Supplementary Information, **Figure S7**). **Figure 4D** exhibits a representative TEM image of the harvested samples after 10 hours electrolysis in 1 M KOH at 10 mA $cm^{-2}$, where no significant change could be detected compared with the initial Co-V sample.

## 4. Conclusion

In conclusion, we report a breakthrough in the development of cheap, sustainable and efficient amorphous electrocatalysts based on the combination of cobalt with vanadium for the production of hydrogen through water splitting as a renewable energy storage system. With tailoring of the V-content in the cobalt, the electrocatalytic activity was drastically improved with a Tafel slope as low as 66 mV $decade^{-1}$ and a low overpotential of 300 mV achieved at current density of 10 mA $cm^{-2}$. This new synthetic approach introduces a class of promising amorphous materials for use in both alkaline and neutral electrolyzers.


## Acknowledgements

This work was supported by NSERC Discovery and NSERC Strategic Grants (JB).


References


1. Meyer, T. J., *Nature* (2008) **451** (7180), 778
2. Smith, R. D. L., *et al.*, *Science* (2013) **340** (6128), 60
3. Pletcher, D., and Li, X., *International Journal of Hydrogen Energy* (2011) **36** (23), 15089
4. Amaral, L., *et al.*, *Journal of The Electrochemical Society* (2017) **164** (4), F427
5. Santos, D. M. F., *et al.*, *Química Nova* (2013) **36**, 1176
6. McCrory, C. C. L., *et al.*, *Journal of the American Chemical Society* (2015) **137** (13), 4347
7. Carmo, M., *et al.*, *International Journal of Hydrogen Energy* (2013) **38** (12), 4901
8. Frame, F. A., *et al.*, *Journal of the American Chemical Society* (2011) **133** (19), 7264

9. Burke, M. S.*, et al.*, *Chemistry of Materials* (2015)
10. McCrory, C. C. L.*, et al.*, *Journal of the American Chemical Society* (2013) **135** (45), 16977
11. Liu, B.*, et al.*, *ACS Applied Materials & Interfaces* (2016) **8** (28), 18577
12. Liu, B.*, et al.*, *Advanced Materials* (2017) **29** (19), 1606521
13. Liu, B.*, et al.*, *Small* (2017) **13** (43), 1701875
14. Zhao, Y.*, et al.*, *Scientific Reports* (2015) **5**, 7629
15. Bergmann, A.*, et al.*, *Nat Commun* (2015) **6**
16. He, J.*, et al.*, *Electrochimica Acta* (2014) **119**, 64
17. Liu, X.*, et al.*, *Chemistry of Materials* (2014) **26** (5), 1889
18. Li, Y.*, et al.*, *Advanced Materials* (2010) **22** (17), 1926
19. Karlin, K. D., *Progress in Inorganic Chemistry*. Wiley: 2011
20. Doyle, R. L.*, et al.*, *Physical Chemistry Chemical Physics* (2013) **15** (33), 13737
21. Zeng, K., and Zhang, D., *Progress in Energy and Combustion Science* (2010) **36** (3), 307
22. Binninger, T.*, et al.*, *Scientific Reports* (2015) **5**, 12167
23. Chang, S. H.*, et al.*, *Nat Commun* (2014) **5**
24. Roger, I., and Symes, M. D., *Journal of the American Chemical Society* (2015) **137** (43), 13980
25. Kanan, M. W., and Nocera, D. G., *Science* (2008) **321** (5892), 1072
26. Kanan, M. W.*, et al.*, *Chemical Society Reviews* (2009) **38** (1), 109
27. Esswein, A. J.*, et al.*, *Energy & Environmental Science* (2011) **4** (2), 499
28. Tsuji, E.*, et al.*, *Electrochimica Acta* (2011) **56** (5), 2009
29. Windisch, C. F.*, et al.*, *Thin Solid Films* (2001) **398**, 45
30. Burkhardt, W.*, et al.*, *Thin Solid Films* (1999) **345** (2), 229
31. Batista, C.*, et al.*, *Journal of Nanoscience and Nanotechnology* (2009) **9** (7), 4220
32. Manning, T. D.*, et al.*, *Journal of Materials Chemistry* (2005) **15** (42), 4560
33. Batista, C.*, et al.*, *Journal of Nanoscience and Nanotechnology* (2011) **11** (10), 9042
34. Hanlon, T. J.*, et al.*, *Thin Solid Films* (2003) **436** (2), 269
35. Wu, Y.*, et al.*, *Scientific Reports* (2015) **5**, 9328
36. Deganello, F.*, et al.*, *Journal of the European Ceramic Society* (2009) **29** (3), 439
37. Esswein, A. J.*, et al.*, *The Journal of Physical Chemistry C* (2009) **113** (33), 15068
38. Lu, Z.*, et al.*, *Nat Commun* (2014) **5**
39. Zhang, X.*, et al.*, *ACS Applied Materials & Interfaces* (2015) **7** (39), 21745
40. Chen, S., and Qiao, S.-Z., *ACS Nano* (2013) **7** (11), 10190
41. Liu, G.*, et al.*, *Advanced Energy Materials* (2016) **6** (15), 1600697
42. Tüysüz, H.*, et al.*, *Nano Res.* (2013) **6** (1), 47
43. Liang, Y.*, et al.*, *Nat Mater* (2011) **10** (10), 780
44. Wu, J.*, et al.*, *Nano Res.* (2012) **5** (8), 521
45. Trotochaud, L.*, et al.*, *Journal of the American Chemical Society* (2012) **134** (41), 17253
46. Wang, Y.*, et al.*, *Advanced Energy Materials* (2014) **4** (16), n/a
47. Zhou, X.*, et al.*, *ACS Applied Materials & Interfaces* (2015) **7** (36), 20322
48. Wang, Y.*, et al.*, *Chemical Communications* (2014) **50** (98), 15529
49. Zhao, W.*, et al.*, *ACS Nano* (2014) **8** (10), 10909
50. Nikolov, I.*, et al.*, *Journal of Electroanalytical Chemistry* (1997) **429** (1–2), 157
51. Singh, R. N.*, et al.*, *Electrochemistry Communications* (2007) **9** (6), 1369
52. Anantharaj, S.*, et al.*, *Journal of Materials Chemistry A* (2015) **3** (48), 24463
53. Lu, X., and Zhao, C., *Nat Commun* (2015) **6**
54. Burke, M. S.*, et al.*, *Chemistry of Materials* (2015) **27** (22), 7549

55. Yang, J.*, et al.*, *The Journal of Physical Chemistry C* (2010) **114** (1), 111
56. Makhlouf, M. T.*, et al.*, *Journal of Nanoparticles* (2013) **2013**, 7
57. Harreld, J. H.*, et al.*, *International Journal of Inorganic Materials* (1999) **1** (2), 135
58. Xu, Q.-Z.*, et al.*, *Current Nanoscience* (2014) **11** (1), 107

**We report a mixed vanadium cobalt electrocatalyst, with an unprecedentedly low overpotential for the $O_2$ evolution reaction in both at neutral and alkaline pH, outperforming $IrO_2$ and a recently discovered cobalt phosphate catalyst in terms of both OER activity and stability.**

Keyword Oxygen evolution reaction, cobalt, vanadium, water oxidation,

alkaline, neutral, catalysis

Geraldine Merle, Isaac Abrahams, Jake Barralet*

**Powerful amorphous mixed metal catalyst for efficient water-oxidation**

# Supporting Information

**Powerful amorphous mixed metal catalyst for efficient water-oxidation**

Geraldine Merle, Isaac Abrahams, Jake Barralet*

**Figure S1.** Catalytic activity and stability plots. The x-axis represents the overpotential needed to achieve 10 mA $cm^{-2}$ at $t = 0$. The y-axis represents the overpotential needed to reach 10 mA $cm^{-2}$ at $t = 2$ hours (adapted from[10])

**Figure S2**. **(A)** Tafel curves of Co-V and Co control catalyst in 1 M KOH with iR correction and **(B)** Nyquist plot of Co control catalyst and Co-V catalyst using glycine as fuel at AC amplitude of 2.5 and 5 mA $cm^{-2}$, in 1M KOH vs. Ag/AgCl from 100 kHz to 0.1Hz.

**Figure S3**. SEM images of the electrocatalyst deposited on glassy carbon materials before (A) and after (B) chronocoulometry measurement with associated elemental mapping of Co, V and O elements. (C) Low and high magnification HR-TEM images of Co-V catalyst after long term stability measurement (and associate Selected Area Electron Diffraction) and EDX analysis.

**Figure S4**. Remaining electrocatalytic activity of Co-V catalyst after storage in 6 M KOH solution at 80 °C

**Figure S5**. (**A**) Linear sweep voltammograms (LSVs) of control and Co-V catalyst at different Co:V ratios, prepared by using glycine as fuel, at scan rate of 20mV $s^{-1}$ in 1M KOH. The Co-V catalysts exhibit a significantly higher catalytic current than control catalyst, with an OER onset overpotential of around 0.3 V and 0.4 V for the Co-V catalyst and Co control respectively. The mass ratio 5:1 $Co(NO_3)_2$:$VOSO_4$ seems to produce the more electro catalytically active materials towards OER. (**B**) LSV of control and Co-V catalyst at a 5:1 Co:V ratio at a scan rate of 20 mV $s^{-1}$ in 1 M KOH at various temperatures. (**C**) SEM images of Co-V catalysts at different Co:V ratios. Particles exhibit an irregular shape suggestive of a glassy material, with V incorporation V increasing the size of particles.

**Figure S6**. SEM micrograph of Co-V catalyst 5:1 (Top left) associated with EDX analyses of round sphere (top right), platelet (bottom left) and granules (bottom right)

**Figure S7**. **(A)** XRD of Co control catalyst, and **(B)** Co-V catalyst after annealing at 600 °C. **(C)** Low magnification TEM image of Co-V (and associate Selected Area Electron Diffraction) and **(D)** XPS of Co in $Co_3O_4$ electrocatalyst[58]

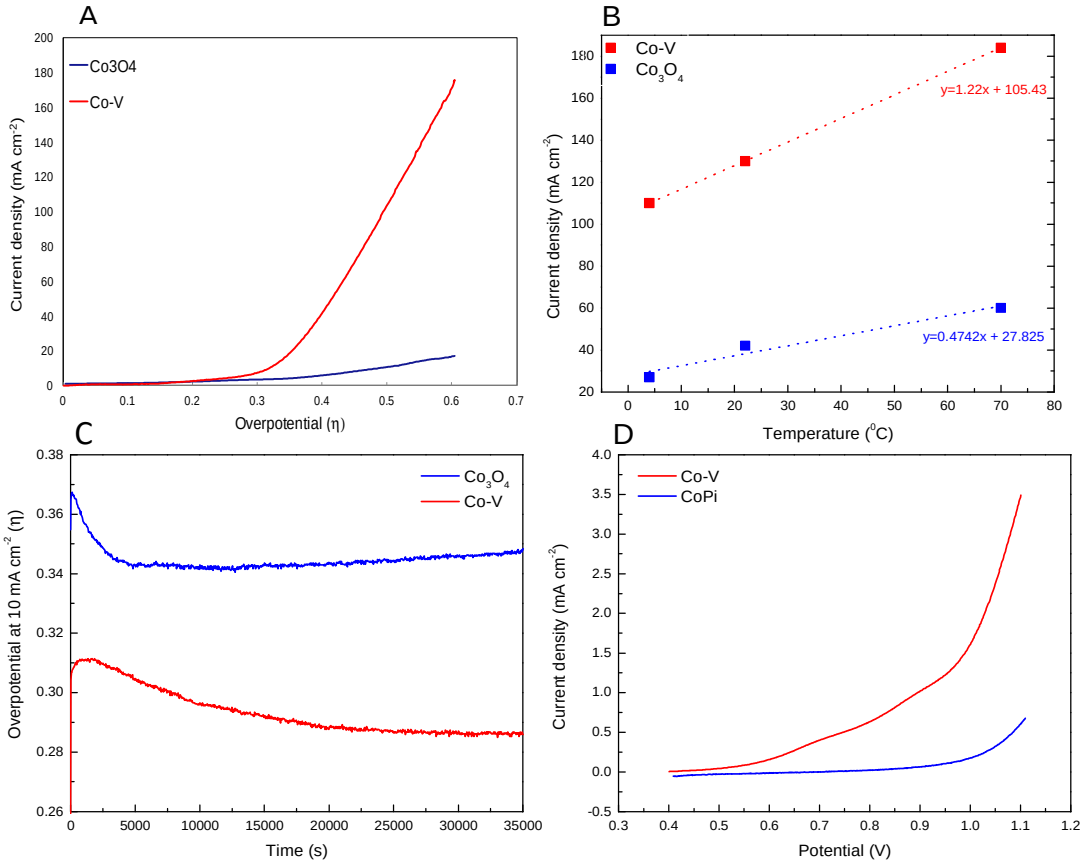


**Figure 1. (A)** Cyclic voltammograms of $Co_3O_4$ control catalyst and Co-V catalyst. The x-axis is the overpotential vs. Ag/AgCl and y-axis represents the current density in mA $cm^{-2}$, at 20 mV $s^{-1}$ in 1 M KOH at 25 °C. **(B)** Temperature dependence of the catalytic current for Co control catalyst and Co-V catalyst in 1 M KOH. **(C)** Chronopotentiometric plot of Co control catalyst and Co-V catalyst at 10 mA $cm^{-2}$ in 1 M KOH at 25 °C. **(D)** Linear sweep voltammetry at a scan rate of 20 mV s, in 0.1 M phosphate buffer pH 7.4 at 25 °C.

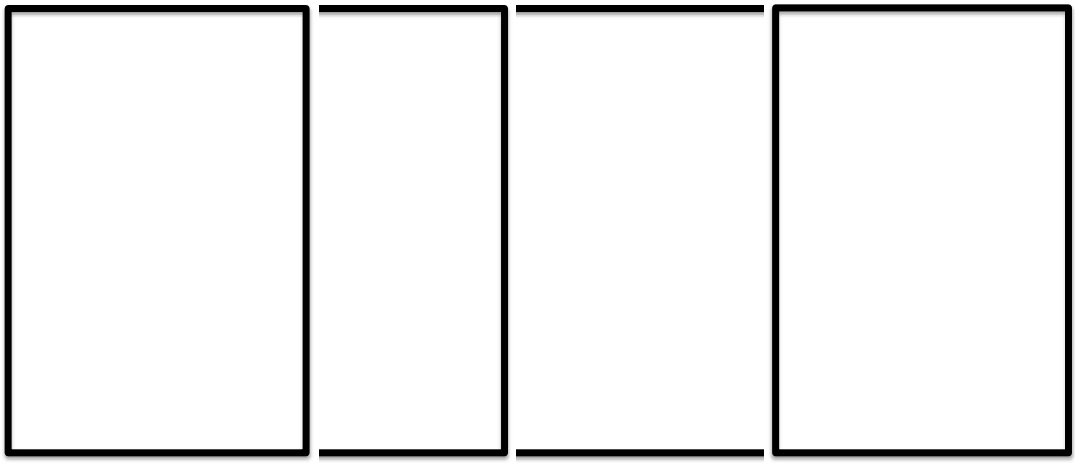

**Figure 2**. **(A)** Top to bottom (Left: control and Right: Co-V): Starting solutions, after the 1st drying step and finally the calcined foam obtained after pyrolysis. **(B)** Pictures of the final electrocatalytic material (top: control and bottom: Co-V). **(C)** SEM micrographs of the control and **(D)** Co-V catalysts. Elemental mapping of the Co-V materials with (E, yellow) Co and (F, blue) V elements. The elemental map signals were obtained by scanning a square of the Co-V image.

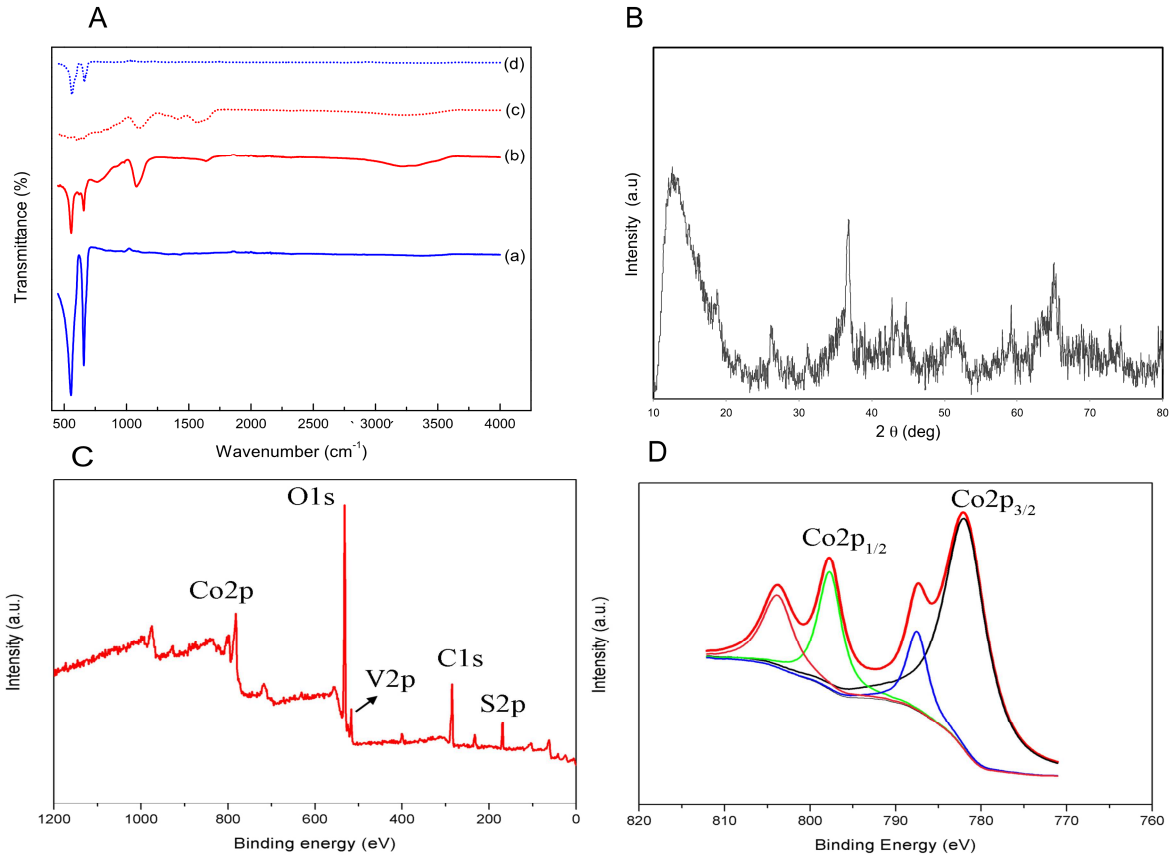


**Figure 3. (A)** FTIR of Co-V catalyst and Co control catalyst before (a and c) and after (b and d) heat treatment at 600˚C, **(B)** XRD of Co-V catalyst (XRD of Co-control catalyst in Supplementary Information, **Figure S6** A), **(C)** XPS survey and **(D)** XPS spectra of the Co element.

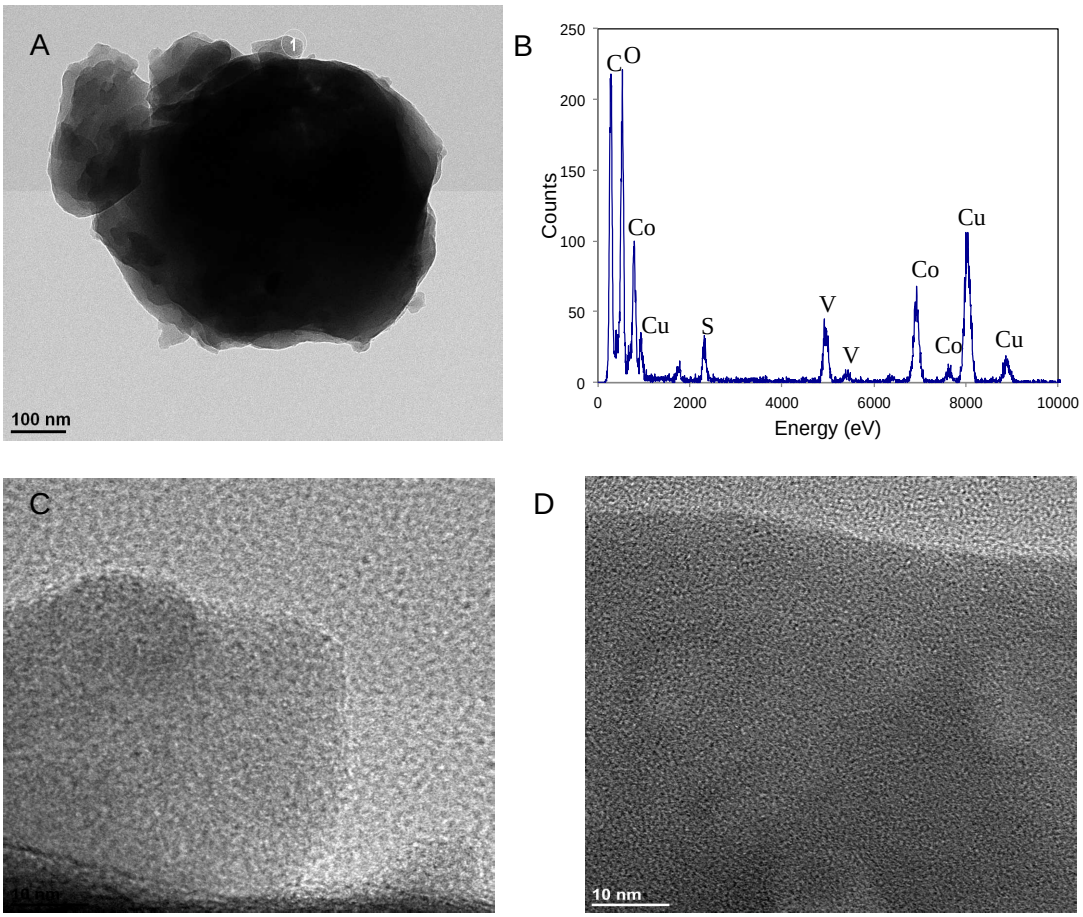


**Figure 4**. TEM images of a Co-V sample, **(A)** Low magnification TEM image of a Co-V sample, **(B)** representative EDS spectrum and **(C)** HR-TEM image of an individual platelet. **(D)** HRTEM image of an individual platelet after 10 h subjected to electrolysis.

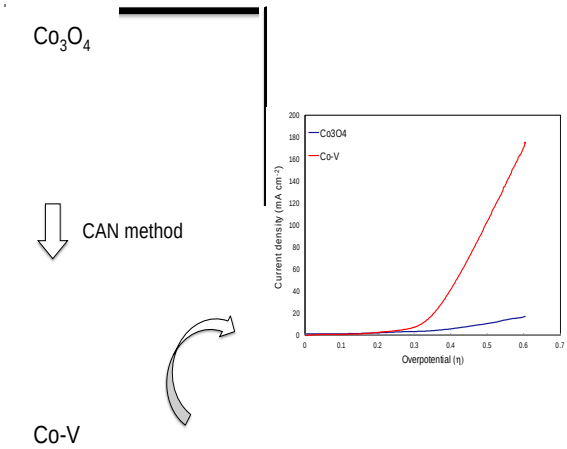

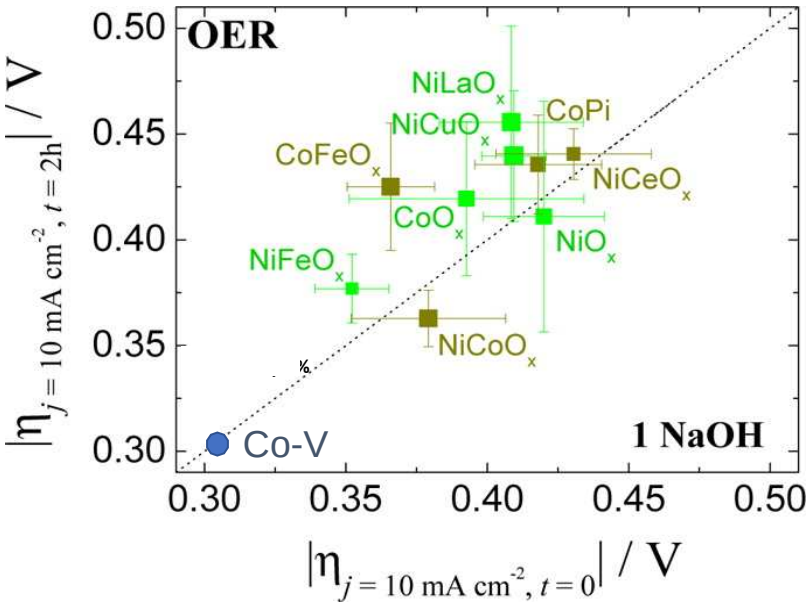


**Figure S1.** Catalytic activity and stability plots. The x-axis represents the overpotential needed to achieve 10 mA cm$^{-2}$ at $t$ = 0. The y-axis represents the overpotential needed to reach 10 mA cm$^{-2}$ at $t$ = 2 hours (adapted from[10])

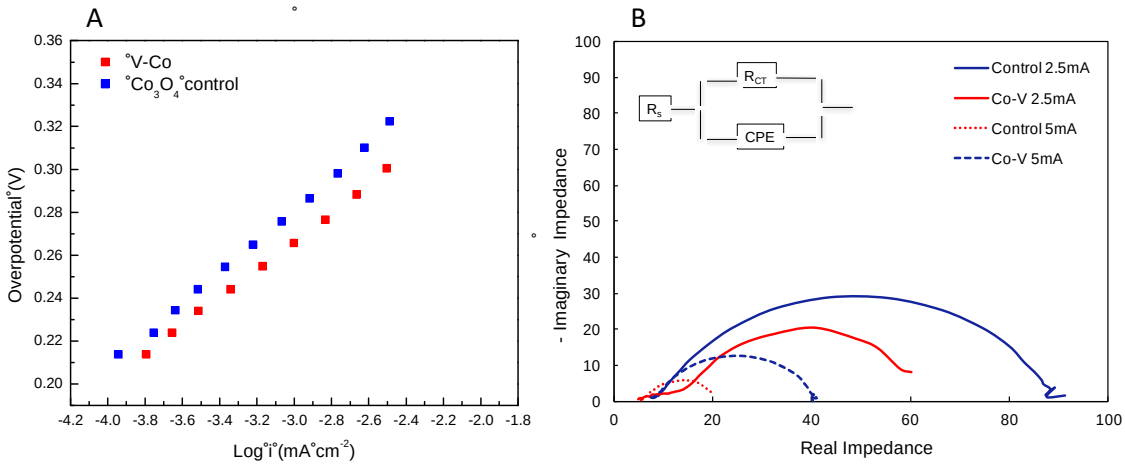


**Figure S2**. **(A)** Tafel curves of Co-V and Co control catalyst in 1 M KOH with iR correction and **(B)** Nyquist plot of Co control catalyst and Co-V catalyst using glycine as fuel at AC amplitude of 2.5 and 5 mA cm$^{-2}$, in 1M KOH vs. Ag/AgCl from 100 kHz to 0.1Hz.

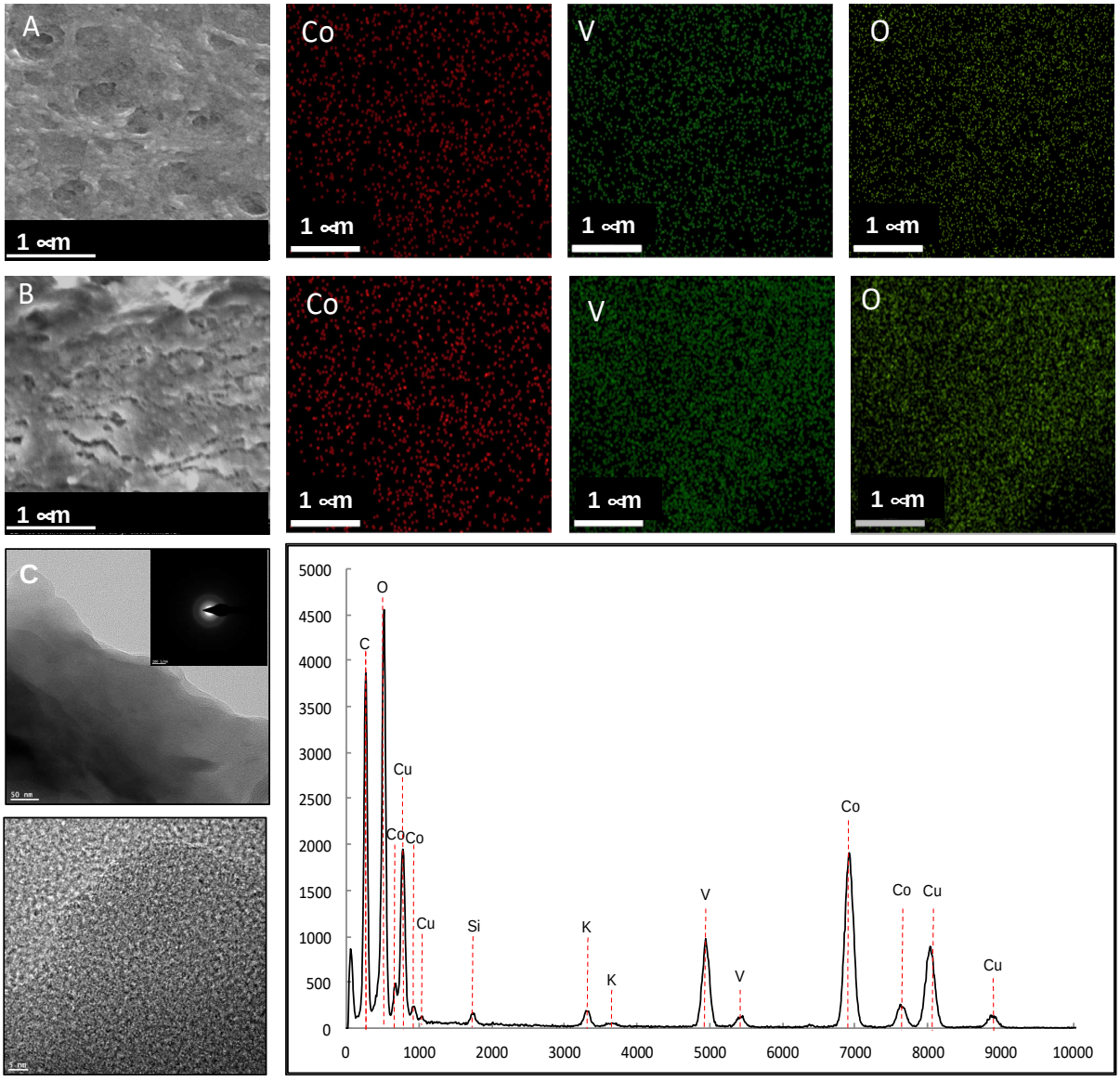


**Figure S3**. SEM images of the electrocatalyst deposited on glassy carbon materials before (A) and after (B) chronocoulometry measurement with associated elemental mapping of Co, V and O elements. (C) Low and high magnification HR-TEM images of Co-V catalyst after long term stability measurement (and associate Selected Area Electron Diffraction) and EDX analysis.

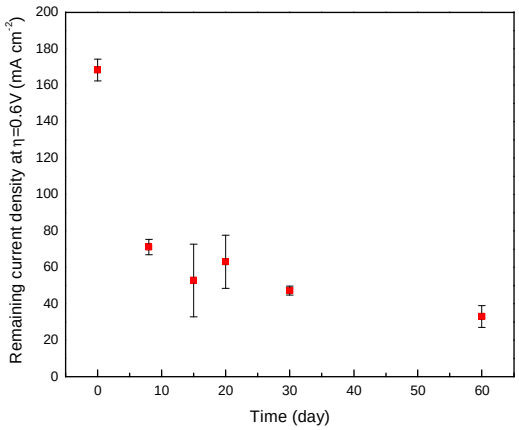


**Figure S4**. Remaining electrocatalytic activity of Co-V catalyst after storage in 6 M KOH solution at 80 °C

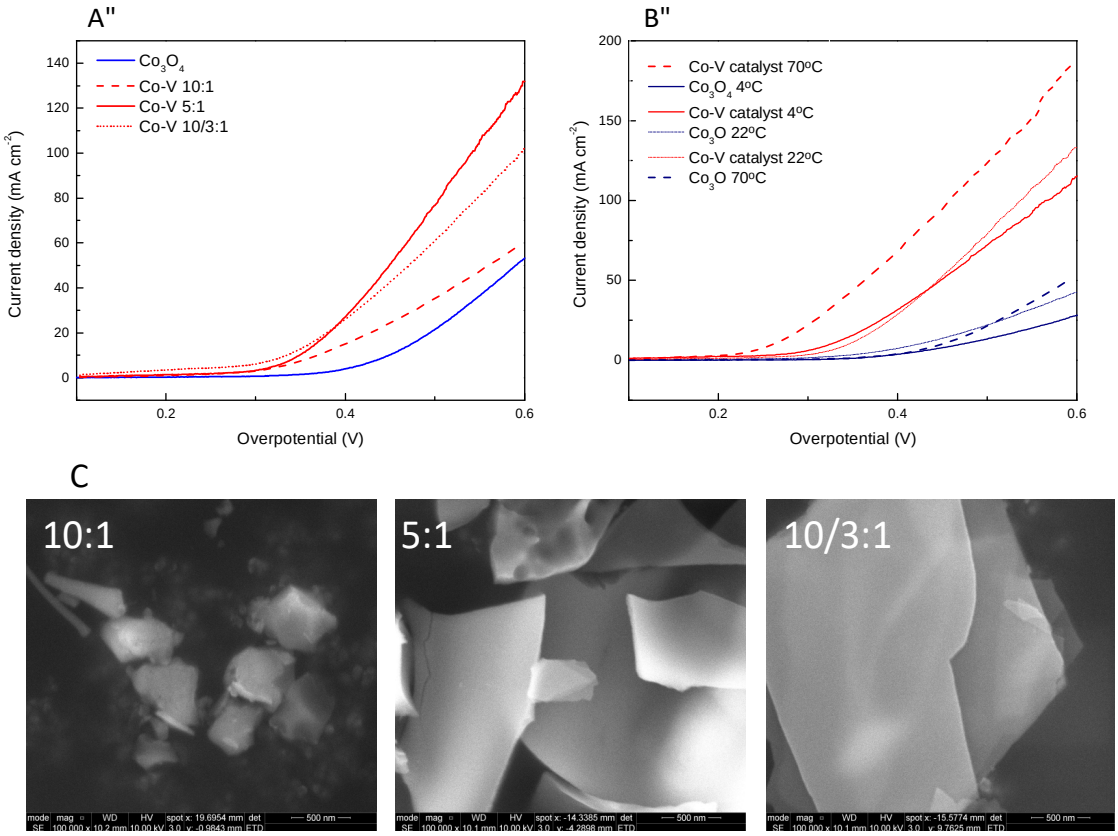


**Figure S5**. (**A**) Linear sweep voltammograms (LSVs) of control and Co-V catalyst at different Co:V ratios, prepared by using glycine as fuel, at scan rate of 20mV $s^{-1}$ in 1M KOH.

The Co-V catalysts exhibit a significantly higher catalytic current than control catalyst, with an OER onset overpotential of around 0.3 V and 0.4 V for the Co-V catalyst and Co control respectively. The mass ratio 5:1 $Co(NO_3)_2$:$VOSO_4$ seems to produce the more electro catalytically active materials towards OER. (**B**) LSV of control and Co-V catalyst at a 5:1 Co:V ratio at a scan rate of 20 mV $s^{-1}$ in 1 M KOH at various temperatures. (**C**) SEM images of Co-V catalysts at different Co:V ratios. Particles exhibit an irregular shape suggestive of a glassy material, with V incorporation V increasing the size of particles.

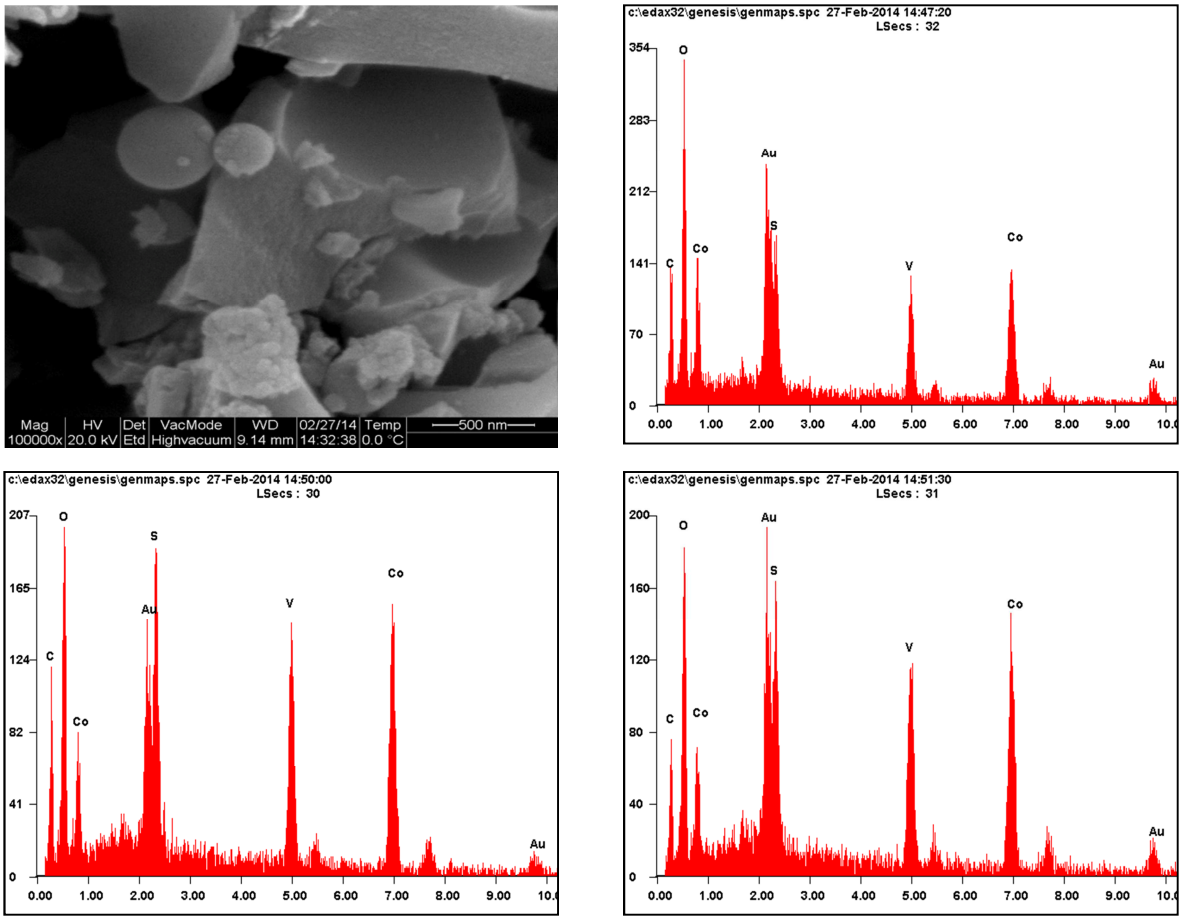


**Figure S6**. SEM micrograph of Co-V catalyst 5:1 (Top left) associated with EDX analyses of round sphere (top right), platelet (bottom left) and granules (bottom right)

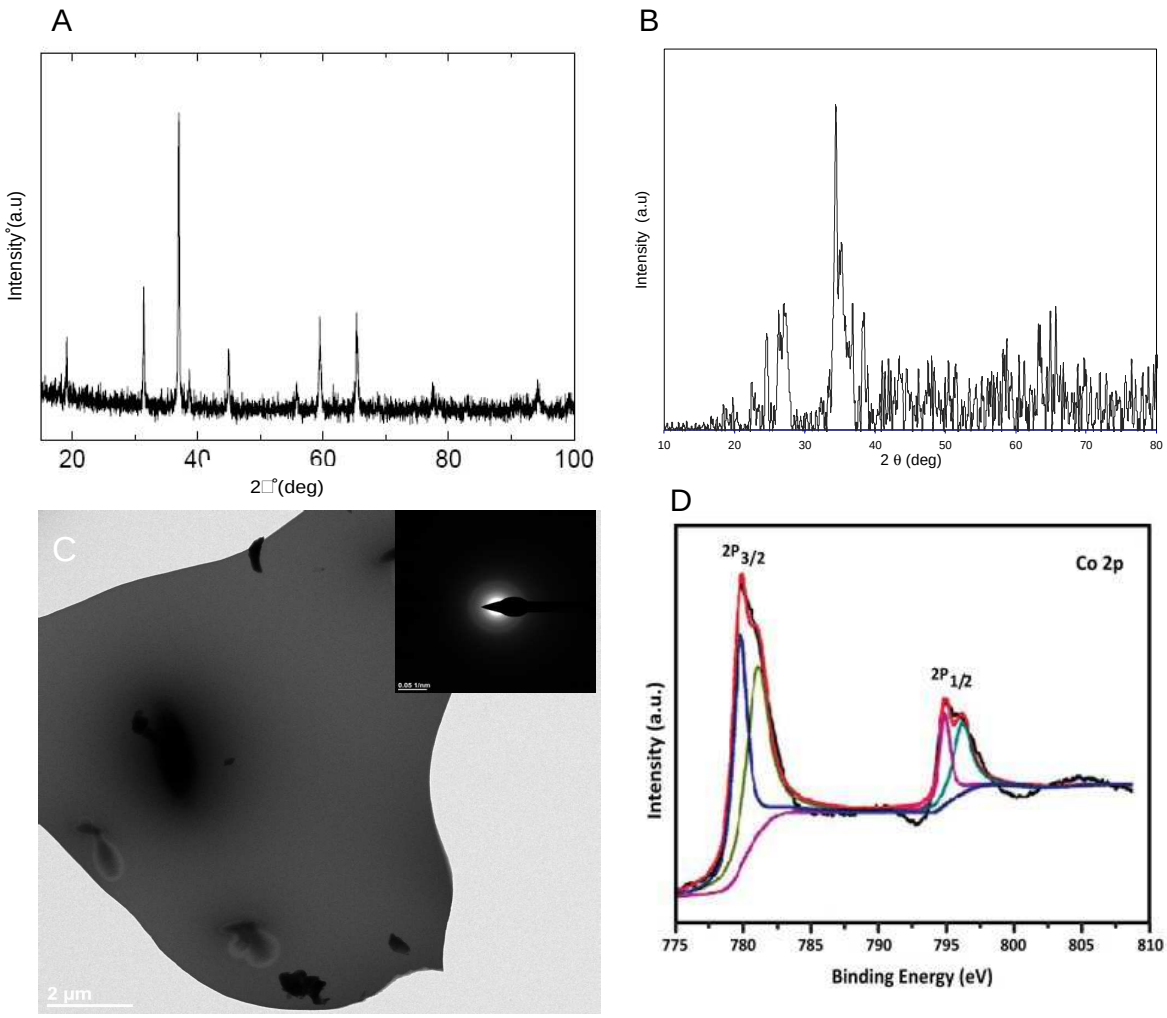


**Figure S7**. **(A)** XRD of Co control catalyst, and **(B)** Co-V catalyst after annealing at 600 °C. **(C)** Low magnification TEM image of Co-V (and associate Selected Area Electron Diffraction) and **(D)** XPS of Co in $Co_3O_4$ electrocatalyst[58]

Supporting Information

**Powerful amorphous mixed metal catalyst for efficient water-oxidation**

Geraldine Merle, Isaac Abrahams, Jake Barralet*

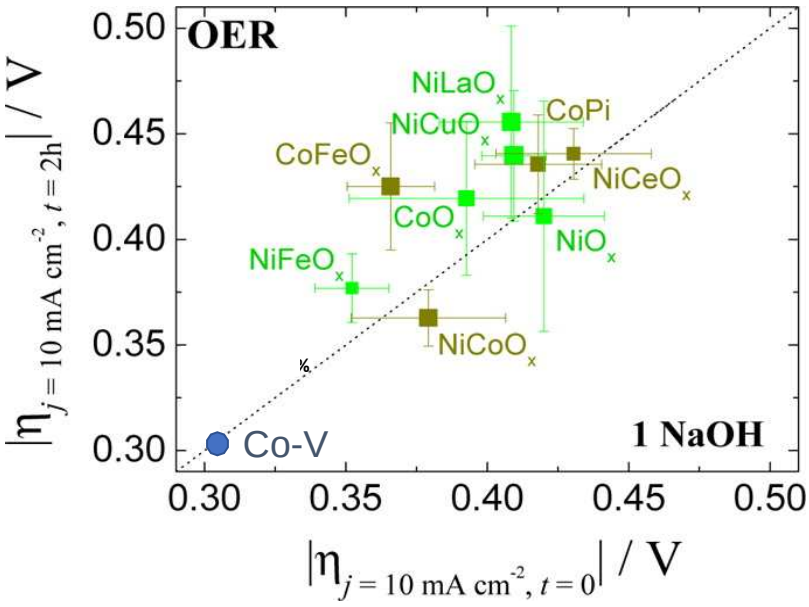


**Figure S1.** Catalytic activity and stability plots. The x-axis represents the overpotential needed to achieve 10 mA cm$^{-2}$ at $t$ = 0. The y-axis represents the overpotential needed to reach 10 mA cm$^{-2}$ at $t$ = 2 hours (adapted from[10])

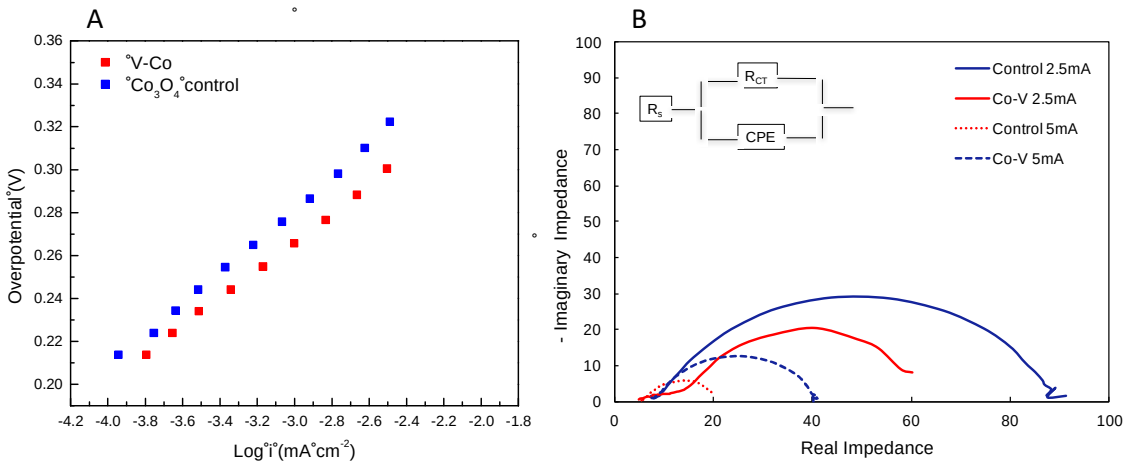


**Figure S2**. **(A)** Tafel curves of Co-V and Co control catalyst in 1 M KOH with iR correction and **(B)** Nyquist plot of Co control catalyst and Co-V catalyst using glycine as fuel at AC amplitudes of 2.5 and 5 mA $cm^{-2}$, in 1M KOH vs. Ag/AgCl from 100 kHz to 0.1Hz.

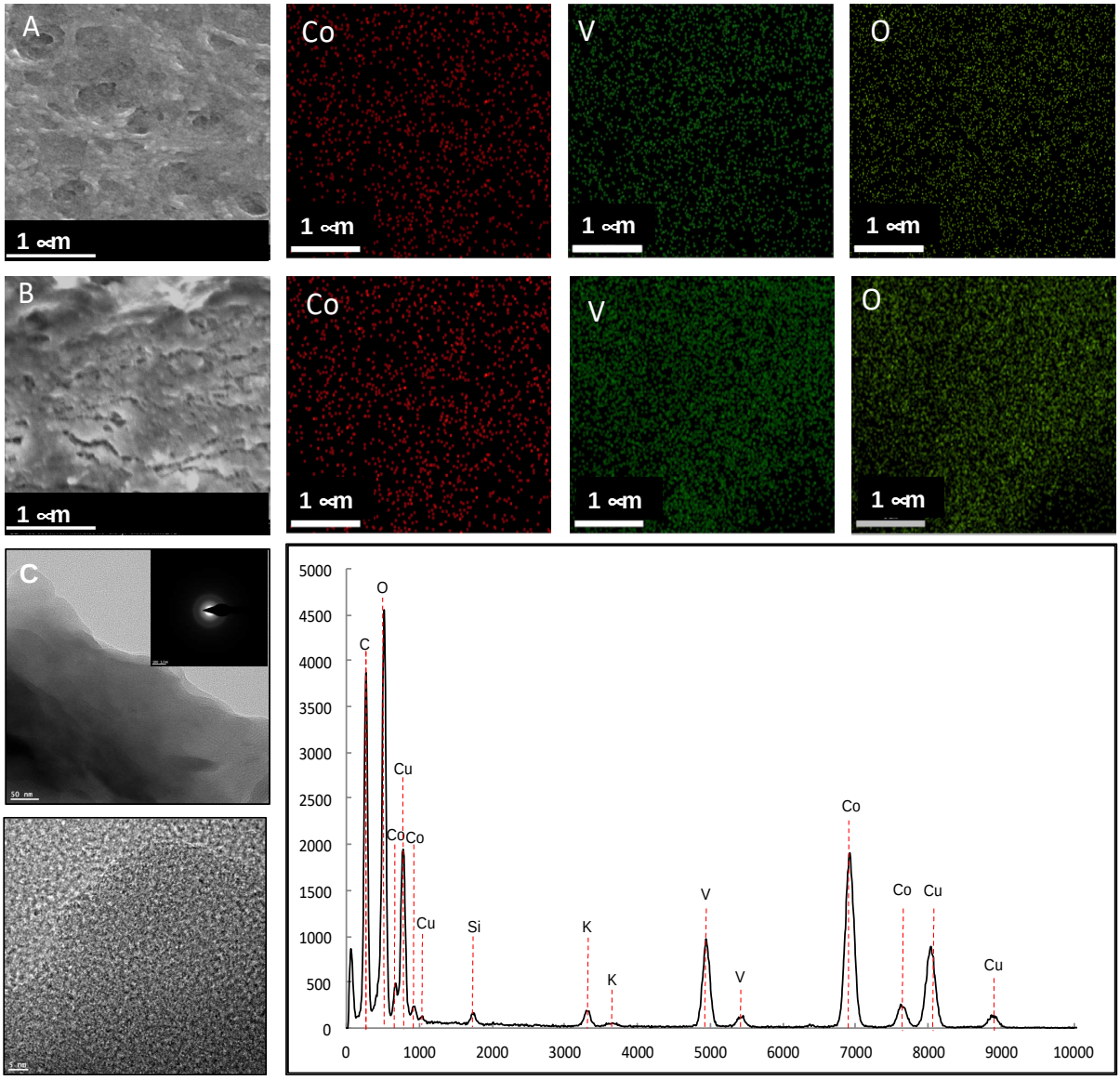


**Figure S3**. SEM images of the electrocatalyst deposited on glassy carbon materials before (A) and after (B) chronocoulometry measurement with associated elemental mapping of Co, V and O elements. (C) Low and high magnification HR-TEM images of Co-V catalyst after long term stability measurement (and associate Selected Area Electron Diffraction) and EDX analysis.

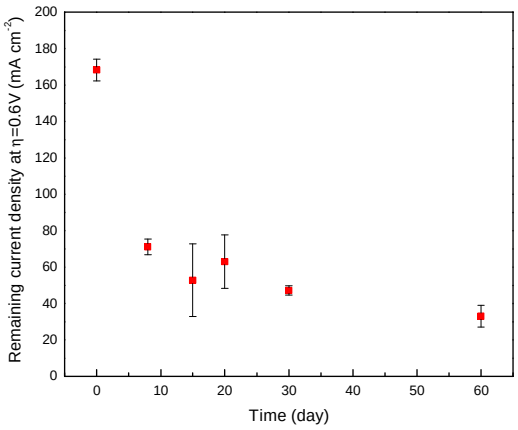


**Figure S4**. Remaining electrocatalytic activity of Co-V catalyst after storage in 6 M KOH solution at 80 °C

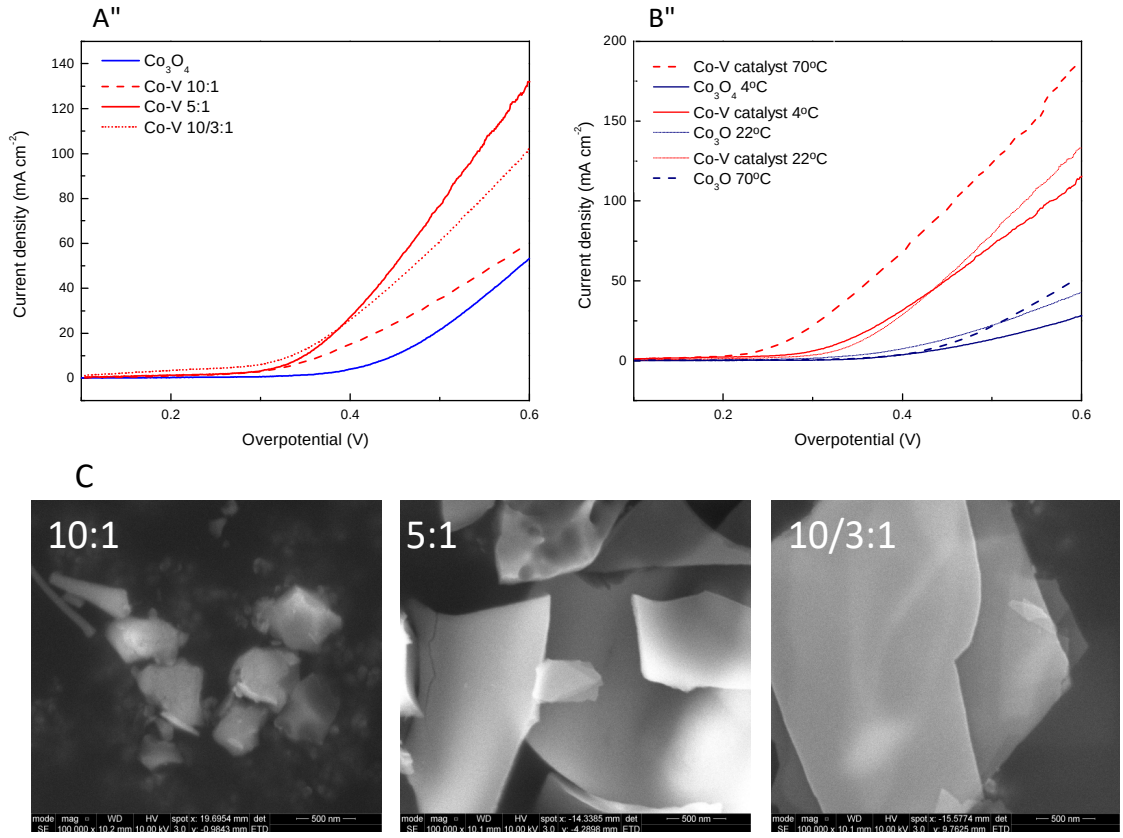


**Figure S5**. (**A**) Linear sweep voltammograms (LSVs) of control and Co-V catalyst at different Co:V ratios, prepared by using glycine as fuel, at scan rate of 20 mV $s^{-1}$ in 1 M KOH. The Co-V catalysts exhibit a significantly higher catalytic current than control catalyst, with an OER onset overpotential of around 0.3 V and 0.4 V for the Co-V catalyst and Co control respectively. The mass ratio 5:1 $Co(NO_3)_2$:$VOSO_4$ seems to produce the more electro catalytically active materials towards OER. (**B**) LSV of control and Co-V catalyst at a 5:1 Co:V ratio at a scan rate of 20 mV $s^{-1}$ in 1 M KOH at various temperatures. (**C**) SEM images of Co-V catalysts at different Co:V ratios. Particles exhibit an irregular shape suggestive of a glassy material, with V incorporation V increasing the size of particles.

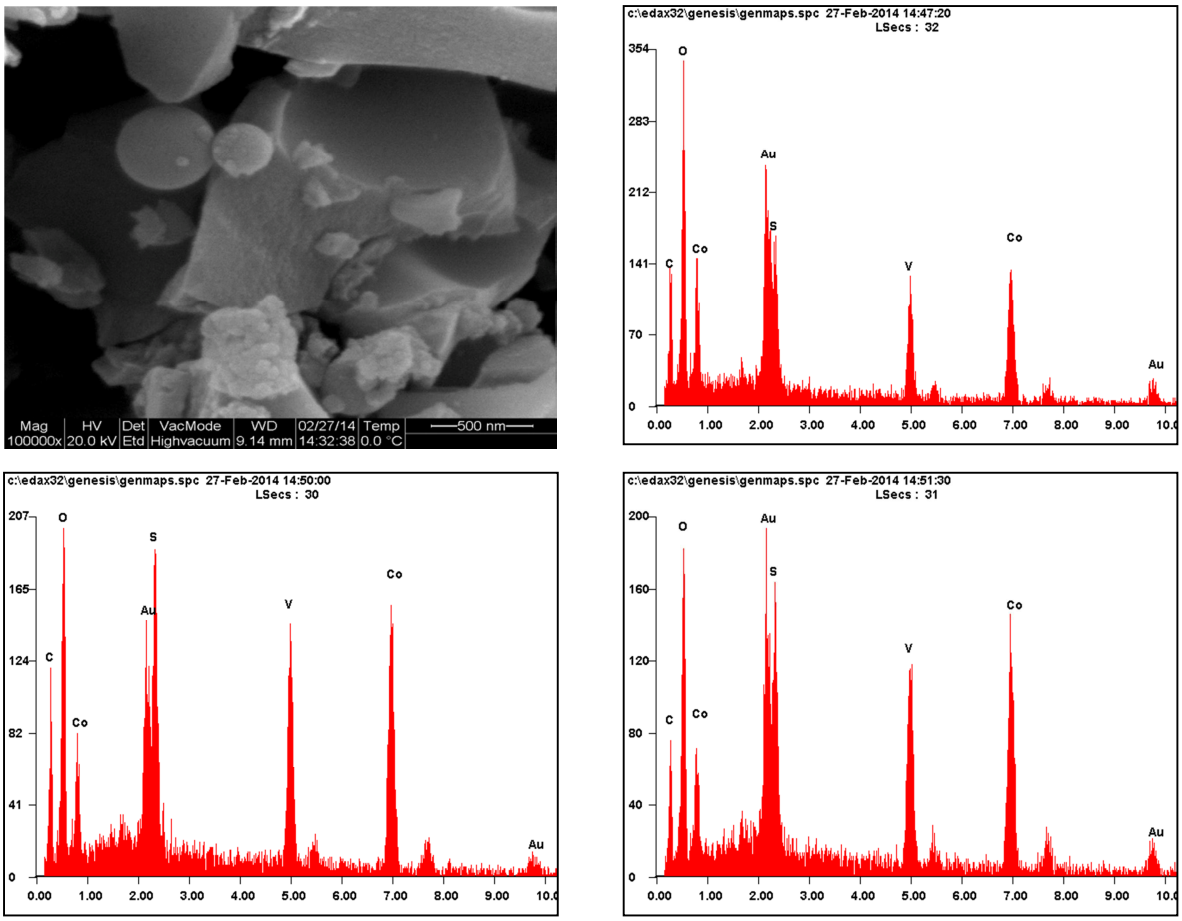


**Figure S6**. SEM micrograph of Co-V catalyst 5:1 (Top left) with associated EDX analyses of round sphere (top right), platelet (bottom left) and granules (bottom right)

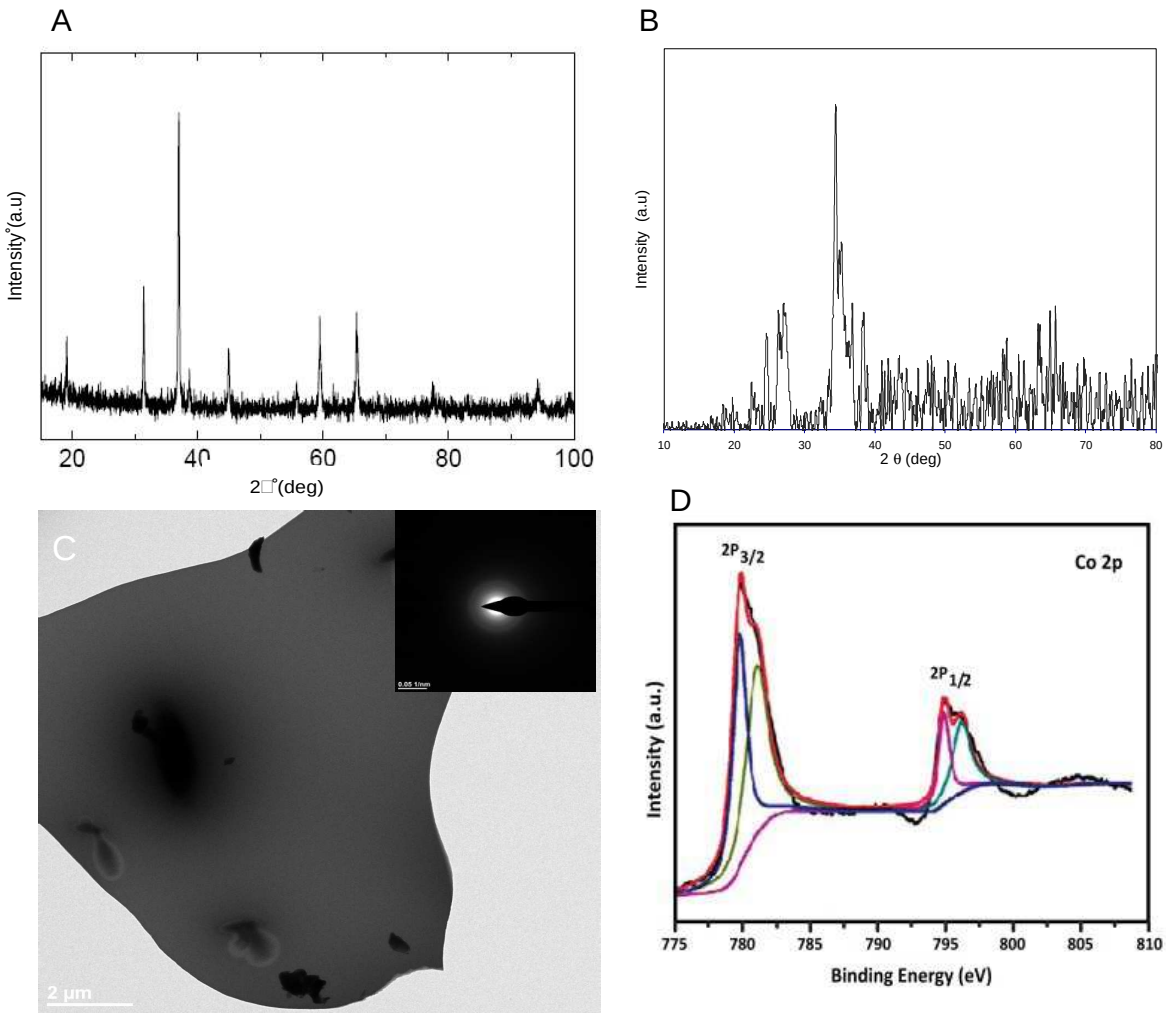


**Figure S7**. **(A)** XRD of Co control catalyst, and **(B)** Co-V catalyst after annealing at 600 °C. **(C)** Low magnification TEM image of Co-V (and associate Selected Area Electron Diffraction) and **(D)** XPS of Co in $Co_3O_4$ electrocatalyst[61]

[61] Q.-Z. Xu, et al., Curr. Nanosci. 11 (1) (2014) 107.